

Modeling and Control of Heating and Heat Circulation in Direct Air Capture System

Paajanen Antti, Nevaranta Niko, Bajamundi Cyril

This is a Publisher's version version of a publication
published by Elsevier
in Chemical Engineering Science

DOI: 10.1016/j.ces.2024.120745

Copyright of the original publication:

© 2024 The Authors.

Please cite the publication as follows:

Antti Paajanen, Niko Nevaranta, Cyril Bajamundi, Modeling and Control of Heating and Heat Circulation in Direct Air Capture System, Chemical Engineering Science, 2024, 120745, ISSN 0009-2509, <https://doi.org/10.1016/j.ces.2024.120745>.

**This is a parallel published version of an original publication.
This version can differ from the original published article.**



Modeling and control of heating and heat circulation in direct air capture system

Antti Paajanen^{a,b,*}, Niko Nevaranta^b, Cyril Bajamundi^c

^a Soletair Power, Tuotantokatu 2, Lappeenranta, 53850, Finland

^b LUT University, Yliopistonkatu 34, Lappeenranta, 53850, Finland

^c VTT Technical Research Center of Finland Ltd., Koivurannantie 1, Jyväskylä, 40400, Finland

ARTICLE INFO

Keywords:

Carbon capture, utilization and storage
FGS-based PI-control
Direct air capture
Adsorbent temperature estimation

ABSTRACT

Direct air capture (DAC) is a critical technology for mitigating climate change. However, the high heat consumption of temperature vacuum swing adsorption (TVSA)-based DAC processes hinders its widespread deployment. This study focuses on developing a control strategy to optimize the energy efficiency of the TVSA heating phase. A novel adsorbent temperature estimation method, validated through experimental data, was integrated into a cascaded PI controller with a fuzzy gain scheduler (FGS). Experimental results demonstrate that the proposed control strategy effectively regulates the heating process, achieving a potential energy saving of up to 14%. This work contributes to enhancing the feasibility and sustainability of DAC technologies.

1. Introduction

The growing interest in carbon capture, utilization, and storage (CCUS) technologies is motivated by the urgent need for cost-effective methods to address global climate challenges by lowering atmospheric carbon dioxide (CO₂) levels. One promising approach is Direct air capture (DAC) technology which is a method of capturing and concentrating CO₂ from ambient air for storage or utilization. Integrating DAC systems into buildings thus creating the possibility of transforming buildings into carbon sinks by permanently storing captured CO₂. Additionally CO₂-lean air supplied to the building can be used to decrease the HVAC energy consumption by decreasing the supplied volume flow of fresh air and adjusting the re-circulation ratio.

Several techniques are used for DAC; for instance, Parvazinia et al. (2018) used amine-functionalized adsorbent as the active material for capture, and Keith et al. (2018), An et al. (2022) employed aqueous alkaline solvent. The recovery of CO₂ from capture media is achievable by applying heat into the process. The amount of heat needed often becomes the dominating factor when evaluating the energy requirement of various DAC processes (House et al., 2011; Baciocchi et al., 2006).

Temperature vacuum swing adsorption (TVSA) is a cyclic process for DAC where heating plays an important phase in the recovery of the captured CO₂. TVSA belongs to a class of DAC techniques called low-temperature solid sorbent systems (LTSS). The National Academies of

Sciences Engineering Medicine (2019) reports that the thermal requirement for LTSS is in the range of 0.944 to 1.333 MWh_{th}/t CO₂ and an electric demand of 0.156 to 0.315 MWh_{el}/t CO₂ in the mid-range (2-4) of their 1-5 (best/worst) scenario scale for solid sorbent DAC. Nevertheless their worst scenario states 1.05 MWh_{el}/t CO₂ and 5.36 MWh_{th}/t CO₂.

In contrast, Stampi-Bombelli et al. (2020) reports that for steam-assisted temperature–vacuum swing adsorption (S-TVSA) systems, the electrical demand around 0.047 to 0.093 MWh_{el}/t CO₂ and 3.333 to 16.667 MWh_{th}/t CO₂ of thermal energy in their simulations, depending on factors such as production rate, desorption pressure, and the amount of steam used.

Therefore significant savings can be made if the thermal or heat requirement is minimized for any LTSS process. By analyzing the open loop TVSA process conditions such as feed flow rate, purge to feed ratio, vacuum level, time of recycle step, etc., have shown that more optimized CO₂ removal processes can be achieved, Jiang et al. (2020) and Lai et al. (2021).

Even though different DAC processes have gained noticeable attention, the closed-loop process control has not been given adequate consideration, which is the motivation for this work. By controlling the TVSA process and the cycles between different process phases, more energy-efficient DAC systems can be achieved especially when the DAC device is installed in a building.

* Corresponding author.

E-mail addresses: antti.paajanen@soletairpower.fi (A. Paajanen), niko.nevaranta@lut.fi (N. Nevaranta), cyril.bajamundi@vtt.fi (C. Bajamundi).

<https://doi.org/10.1016/j.ces.2024.120745>

Received 8 April 2024; Received in revised form 25 July 2024; Accepted 15 September 2024

Available online 17 September 2024

0009-2509/© 2024 The Authors. Published by Elsevier Ltd. This is an open access article under the CC BY license (<http://creativecommons.org/licenses/by/4.0/>).

1.1. Control strategies and modeling

This paper examines the DAC system by focusing on modeling and control of its heating phase and proposes an additional heat circulation phase to decrease thermal energy input to the system per cycle. The proposed step allows the DAC system to recycle the thermal energy from one bed to another thus effectively lowering the specific energy requirement of the process. This is especially relevant in a building environment where usable waste heat is usually limited. To our knowledge there is no comparable work available focusing on the control of Direct Air Capture processes with solid adsorbent, whereas research on control of CO₂ capture systems has focused on systems for other sources of CO₂, for example, post-combustion capture systems by Wu et al. (2020), Wu et al. (2018), Gutierrez-Ortega et al. (2023) with different capture principles and methodologies.

The choice of control strategy is guided by the necessity for straightforward yet efficient control laws for these systems, which can be adjusted and implemented in the field without an in-depth understanding of control engineering. These strategies also consider the varying environmental conditions of the installation site. Given that adsorbent heating is a relatively predictable process, PI-like control methods are often as effective as more complex strategies such as optimal or intelligent control methods, assuming there is a well-designed and well-tuned virtual sensor providing a stable and accurate estimate for the controller. While more advanced methods offer designers more detailed influence over the MIMO system's behavior, this aspect is not addressed in this paper.

Salvinder et al. (2019) have collected comprehensive collection of different control strategies around Proportional–integral–derivative controller (PID) and Model Predictive Control (MPC) aspects for carbon capture systems mainly focusing on capture from flue gases. In Chen et al. (2019) simple PID control laws are evaluated in process control in solvent-based Post-Combustion Capture (PCC) systems with different control variables and their effect on system response. Modeling and control parts of DAC or PCC Cao (2021) presents the possibilities of neural networks for carbon capture processes, these could have a major impact on the control of more complex process parts like product gas treatment/drying in varying conditions.

In this paper, we propose a cascaded PID-type control law to manage the heating phase of the temperature vacuum swing adsorption (TVSA) process, using the sorbent's average temperature estimate for feedback. The main focus of this paper is on controlling the heating of the sorbent to reach the regeneration temperature and managing the transition from the circulation phase to the heating phase in the DAC system. The proposed control law based on system modeling aims to regulate the process more efficiently to achieve energy savings, when the inner PI-control loop is designed to regulate the thermal energy storage (TES), while the outer control loop employs a fuzzy gain scheduler (FGS)-based PI-control for regulating the sorbent temperature. Therefore, experimental validation focuses on both the dynamic properties of the controller and the comparison of energy consumption under different strategies.

The contents of the paper are organized as follows: Section 2 focuses on the modeling of the DAC process (adsorbent heating dynamics) by applying lumped analysis with a discrete node-based approach with an introduction to the virtual sensor of adsorbent temperature. Section 3 introduces the control approach derived for the system. After that, in Section 4 the experimental results are presented, emphasizing the performance evaluation of the proposed control and virtual sensor, alongside an analysis of energy consumption. Finally Section 5 presents the conclusions of this work.

2. Heating and circulation process

A simplified process diagram of the system is found in Fig. 1. There are three different process loops in the system. The cartridges being

heated are connected to the heating loop (red), and the cartridges being cooled are connected to the cooling loop (blue). Heat is transferred from the hot to cold cartridges using the circulation loop (shown in green). For heating the cartridges, thermal energy storage (TES) is used with an electric heater element, whereas for cooling cartridges a radiator is used to dissipate heat during the cooling phase. A vacuum pump is used to bring the DAC chamber to the desorption pressure before the heating/circulation phase begins. A more detailed view of the experimental system is presented in the supplementary material.

2.1. Modeling of cartridge dynamics

A DAC unit is composed of cartridges filled with adsorbent and enclosed inside a chamber capable of reaching the desired vacuum level for the temperature vacuum swing adsorption (TVSA) process. Each cartridge consists of a cylindrical basket filled with sorbent and a helical pipe embedded in the middle of the bed. This pipe acts as a heat exchanger for heating and cooling the sorbent, depending on the state of the TVSA cycle. In this paper, the modeling focus is on the thermal dynamics of the cartridges. Dimensionless parameters in per-unit (pu) are utilized for developing the models and control laws. For example, the target sorbent temperature of the process is set at 1 pu.

The effectiveness of lumped analysis is often limited by the heterogeneity (non-uniformity) of the system being modeled. This can lead to significant temperature gradients within the system, compromising the accuracy of the analysis. To address this limitation and improve flexibility of model, the cartridge can be divided into separate nodes, as shown in Fig. 2. A similar discrete node-based approach has been used by Nash et al. (2017), Bastida et al. (2019), and Bird and Jain (2020) for TES modeling.

Heating of the TES is done by a submerged electric resistance heating element. The average heating power is controlled by a PI controller with a Programmable Logic Controller (PLC). The control principle involves varying the duty cycle, i.e., the duration when the heater is on and off within a five-second interval. The heater element is driven by a solid-state contactor with voltage zero-cross switching.

In this paper, the distances or dimensions of the nodes are divided equally along the cartridge and each node is assumed to have unique dynamics. The cartridge is modeled using single, three, and ten-node models. The dynamical modeling of the cartridge assumes a closed system for the sorbent and an open system for the heat transfer liquids, with a fully developed flow at a steady state.

Each node is divided by the helical pipe-shaped heat exchanger, which separates the sorbent mass into inner and outer regions. The modes of heat transfer methods (i.e., convection, conduction, and radiation) relevant to one node are shown in Fig. 2. Each node has its loss components and can exchange heat with adjacent nodes either through the sorbent masses or via the helical heat exchanger.

The direction of the heat-transfer fluid flow is illustrated in Fig. 2, moving from bottom to top (from node $j + 1$ to 1). Heat transfer within the sorbent mass is assumed to be purely conductive, due to the low porosity of the sorbent bed caused by packing procedure of cartridge and sorbent particle size distribution, with assumption of uniform temperature of adsorbent, when small volume of adsorbent bed is considered. Additionally, the thermal capacitance of the coil heat exchanger is neglected as the exchanger is treated solely as a boundary layer for heat transfer from the flowing liquid to the sorbent mass.

Ultimately, the primary objective of the model is monitoring the temperatures of inner ($T_{j,in}$) and outer ($T_{j,out}$) sorbent masses, and the liquid within the pipe heat exchanger for each node ($T_{c,j}$). Each node is modeled using three ordinary differential equations (ODEs) that describe the dynamics of nodes, based on the point of interest in the modeling perspective.

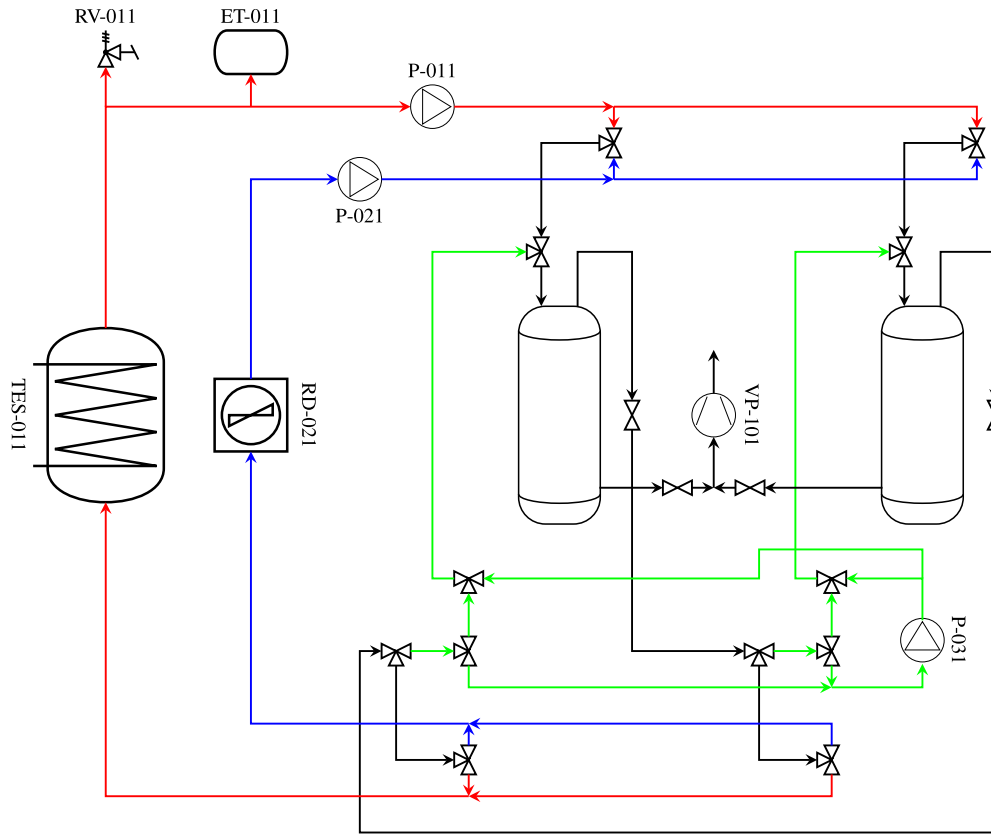


Fig. 1. Generalized process diagram of the circulation and heating system. The abbreviations are as follows: RV stands for relief valve, P for pump, RD for radiator, VP for vacuum pump, ET for expansion vessel, and TES for thermal energy storage.

2.2. Single node dynamics

Following the dynamics illustrated in Fig. 2, the first governing equation representing the liquid temperature Tc_j in the pipe heat exchanger at a certain node j .

$$\frac{dTc_j}{dt} = \frac{\dot{Q}_{j,w,in} - \dot{Q}_{j,w,out} - \dot{Q}_{j,ws,in} - \dot{Q}_{j,ws,out}}{m_{j,w}c_w}, \quad (1)$$

where $\dot{Q}_{j,w,in}$ and $\dot{Q}_{j,w,out}$ represent the heat transfer rates into and out of the node in the heat exchanger, respectively. The terms $\dot{Q}_{j,ws,in}$ and $\dot{Q}_{j,ws,out}$ denote the heat flow from the exchanger to the inner and outer sorbent masses, respectively. Additionally, $m_{j,w}$ represents the mass of the liquid in the node, and c_w is the specific heat of the liquid. The subsequent equations (2) and (3) are derived based on Fig. 2 to describe the dynamics of the inner and outer sorbent masses. To represent the temperature of the outer sorbent mass $T_{j,out}$, the following equation is derived,

$$\frac{dT_{j,out}}{dt} = \frac{\dot{Q}_{j,ws,out} + \dot{Q}_{j+1,out} - \dot{Q}_{j-1,out} - \dot{Q}_{j,loss,out} + \dot{Q}_{j,cross}}{m_{j,s,out}c_s}, \quad (2)$$

where $\dot{Q}_{j+1,out}$ represents the heat transfer to the node from the node below, and $\dot{Q}_{j-1,out}$ represents the heat transfer to the node above. The term $\dot{Q}_{j,loss,out}$ denotes the heat loss from the outer sorbent mass to the ambient, and $\dot{Q}_{j,cross}$ represents the mutual heat transfer between the inner and outer sorbent masses. Additionally, $m_{j,s,out}$ is the mass of the outer sorbent, and c_s is the specific heat of the sorbent. Similarly, the expression for the temperature of the inner sorbent mass $T_{j,in}$ is derived and expressed as follows,

$$\frac{dT_{j,in}}{dt} = \frac{\dot{Q}_{j,ws,in} + \dot{Q}_{j+1,in} - \dot{Q}_{j-1,in} - \dot{Q}_{j,loss,in} - \dot{Q}_{j,cross}}{m_{j,s,in}c_s}. \quad (3)$$

where $m_{j,s,in}$ is the inner sorbent mass. The derived equations illustrate the dynamics of the cartridge's heating state, specifically when heat is supplied to the sorbent. To proceed with the modeling, the next step is to discuss the additional dynamics for the chamber.

2.3. Additional dynamics

The proposed control approach is intended for use in actual industrial DAC products. However, the experimental test environment used in this paper is relatively small compared to a full-scale DAC system, necessitating the inclusion of additional dynamics in the system modeling. These dynamics are experimentally determined and added to the proposed virtual sensor discussed in the next section so that the state space model can also take into account the temperature of the chamber wall.

To identify the chamber wall temperature dynamics a step response is measured from the experimental system, with the temperature sensor encapsulated to the chamber wall, when hot water at the temperature of 1 pu is allowed to flow through the cartridge at 1 pu nominal flow. The identified model is based on a second-order system presented in a standard form

$$\hat{G}_{ch}(s) = \frac{\hat{b}_0}{s^2 + \hat{a}_1s + \hat{a}_0}. \quad (4)$$

A second-order model was chosen for identification due to its representation of a damped response with an initial lag and solely by desire to keep the additional dynamics as simple as possible. The model fitting is performed using the method of moments (MOM) approach for the transfer function model, as reported in Lindh and Nevaranta (2020).

The results for the system studied in this paper are shown in Fig. 3, indicating that the selected model structure represents the dynamical behavior of the chamber (dashed line) and is in a good agreement with the measured step response (red line) and the differentiated impulse

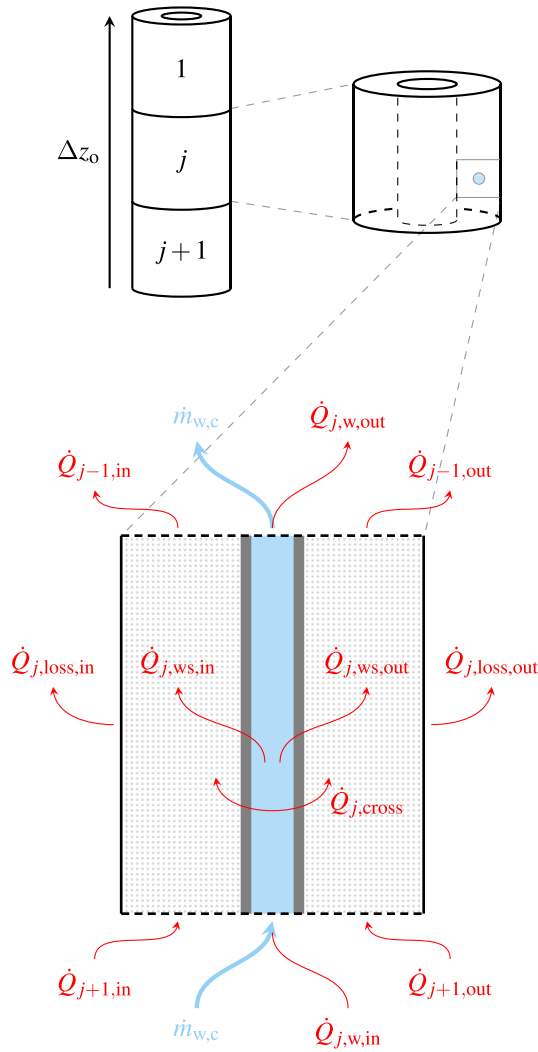


Fig. 2. The cartridge is divided into smaller nodes, with a single node illustrated by the heat flow terms through its boundaries. Heat is applied through the coil to both the inner and outer sorbent masses.

response. Although the identified model does not perfectly describe the behavior, the obtained precision is acceptable due to the much slower dynamics compared to the cartridge model, and its lesser impact on the overall system behavior.

In addition, the cartridges experience heat loss through its supports inside the chamber. These dynamics are discussed further in Section 4. With the identified additional dynamics and the derived node-based differential equations (1) - (3) a multiple-input and multiple-output (MIMO) state-space model can be developed for the three-node system.

Fig. 4 shows the derived node model with and without additional dynamics and the averaged temperature measurements from the testing environment. The model without the added dynamics fails to capture the slow temperature increase observed after 100 minutes, which is due to the warming up of the chamber itself, leading to a steady-state error between the model and the measurements. This result indicates that with the proposed model to represent the additional dynamics, the simulation model is in good agreement with the experimental system and indicates that with a mathematical model with reasonable accuracy, the model-based estimation of the sorbent temperature can be achieved.

It is important to note that in a larger DAC unit, this phenomenon will have a lesser impact due to the significantly larger amount of sorbent compared to the chamber's building material. Meaning that these dynamics are less likely to significantly affect estimator performance in

larger industrial-scale DAC systems, though they are considered in the case studied in this paper.

To compare the testing environment with industrial-sized devices, the thermal masses of the adsorbent and the chamber are calculated, assuming uniform material composition and averaging over the temperature range. For the testing environment, the ratio of thermal mass between the adsorbent and the chamber material is 0.58, whereas, for an industrial-sized DAC chamber, the ratio is 2.1, leading to the assumption that the effect of chamber dynamics is lesser in industrial-sized device.

2.4. Three node model of the cartridge

The previous modeling equations (1)–(3) apply to a single-node system. However, in this paper, the lumped model of the cartridge is expanded to a three-node representation and later on to a ten-node representation for simulation purposes, incorporating additional chamber dynamics. For the sake of clarity, the derivation of the model parameters related to the equations presented in this section is discussed in more detail in supplementary material.

It is important to note that terms in the equations that do not physically exist are neglected. For example, the bottom-most node will not exchange heat with a node below it. In the model, the liquid flow is considered to move from the coil in the bottom node towards the upper nodes (as illustrated in Fig. 2). The expanded set of differential equations for each node is as follows,

$$\begin{aligned} \frac{dT_{c_j}}{dt} &= \frac{C_{w,c}(T_{c_j} - T_{c_{j+1}}) - C_{w,c}(T_{c_{j-1}} - T_{c_j}) - \frac{T_{j,in} - T_{c_j}}{R_{in}} - \frac{T_{j,out} - T_{c_j}}{R_{out}}}{m_{j,w}c_w}, \\ \frac{dT_{j,out}}{dt} &= \frac{\frac{T_{j,out} - T_{c_j}}{R_{out}} - \kappa_{out}(T_{j+1,out} - T_{j,out}) + \kappa_{out}(T_{j,out} - T_{j-1,out})}{m_{j,s,out}c_s} \\ &\quad - \frac{(\delta_{conv,out}(T_{ch} - T_{j,out}) + \delta_{rad,out}(T_{j,out}^4 - T_{ch}^4))\gamma_{loss,cor,out}}{m_{j,s,out}c_s} \\ &\quad + \frac{\kappa_{cc}(T_{j,in} - T_{j,out})}{m_{j,s,out}c_s}, \end{aligned} \quad (5)$$

$$\begin{aligned} \frac{dT_{j,in}}{dt} &= \frac{\frac{T_{j,in} - T_{c_j}}{R_{in}} - \kappa_{in}(T_{j+1,in} - T_{j,in}) + \kappa_{in}(T_{j,in} - T_{j-1,in})}{m_{j,s,in}c_s} \\ &\quad + \frac{-\delta_{cond,in}(T_{j,in} - T_{ch})\gamma_{loss,cor,in} - \kappa_{cc}(T_{j,in} - T_{j,out})}{m_{j,s,in}c_s}. \end{aligned}$$

Where the parameter $C_{w,c} = c_{c,w}\dot{m}_{c,w}$ with $\dot{m}_{c,w}$ representing the mass flow of water in coil. Given the uncertainties and unknown phenomena affecting the dynamics, correction terms $\gamma_{s, cor}$, $\gamma_{loss,in,cor}$ and $\gamma_{loss,out,cor}$ are introduced into the sorbent's thermal conductivity and the loss components for the inner and outer surfaces. The parameters κ_{in} , and κ_{out} represent the physical properties of the system (further detailed in the supplementary material).

By combining the node models described in (5) with the derived additional dynamics, a state-space representation of the system can be formulated. The three-node model is represented as a composition of matrices **A**, **B**, **C**, and **D**, as illustrated in.

$$S_{ys} = \frac{\mathbf{A} \mid \mathbf{B}}{\mathbf{C} \mid \mathbf{D}}$$

The description of state variables, inputs, and outputs are included on the outer edges of the matrix composition for the reader's convenience. For clarity, the matrix cells are shown as coefficients (e.g., $A_{1,1}$ and $B_{2,2}$) in the system representation provided in the next equation (6).

Responses of chamber and identified model

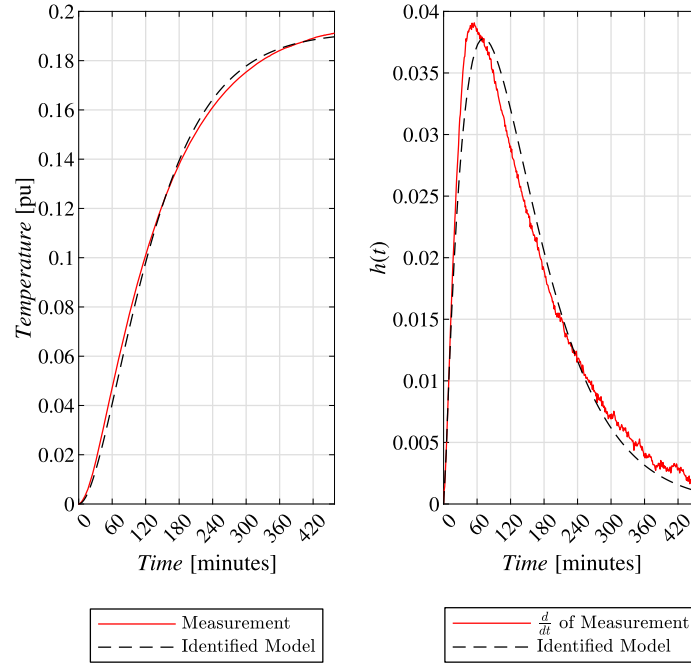


Fig. 3. a) Measured and the identified responses of chamber dynamics and b) differentiated impulse response from the measured step response, compared to the model response.

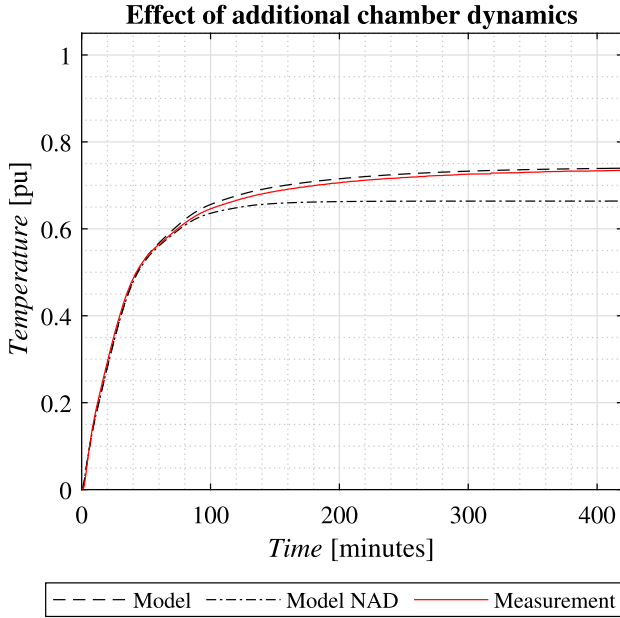


Fig. 4. Averaged measurements and simulated responses of the chamber: with additional dynamics (Model) and without additional dynamics (Model NAD).

$$S_{\text{sys}} = \begin{array}{c|cccccccccccc|cccc|c} A_{1,1} & A_{1,2} & A_{1,3} & A_{1,4} & 0 & 0 & 0 & 0 & 0 & 0 & 0 & 0 & 0 & 0 & 0 & 0 & 0 & 0 & T_{C_1} \\ A_{2,1} & A_{2,2} & A_{2,3} & 0 & A_{2,5} & 0 & 0 & 0 & 0 & 0 & 0 & A_{2,11} & 0 & B_{2,2} & 0 & 0 & 0 & T_{1,\text{out}} \\ A_{3,1} & A_{3,2} & A_{3,3} & 0 & 0 & A_{3,6} & 0 & 0 & 0 & 0 & 0 & A_{3,11} & 0 & B_{2,3} & 0 & 0 & 0 & T_{1,\text{in}} \\ A_{4,1} & 0 & 0 & A_{4,4} & A_{4,5} & A_{4,6} & A_{4,7} & 0 & 0 & 0 & 0 & 0 & 0 & 0 & 0 & 0 & 0 & 0 & T_{C_2} \\ 0 & A_{5,2} & 0 & A_{5,4} & A_{5,5} & A_{5,6} & 0 & 0 & A_{5,8} & 0 & 0 & A_{5,11} & 0 & B_{2,5} & 0 & 0 & 0 & T_{2,\text{out}} \\ 0 & 0 & A_{6,3} & A_{6,4} & A_{6,5} & A_{6,6} & 0 & 0 & A_{6,9} & 0 & A_{6,11} & 0 & 0 & B_{2,6} & 0 & 0 & 0 & T_{2,\text{in}} \\ 0 & 0 & 0 & A_{7,4} & 0 & 0 & A_{7,7} & A_{7,8} & A_{7,9} & 0 & 0 & B_{1,7} & 0 & 0 & 0 & 0 & 0 & 0 & T_{C_3} \\ 0 & 0 & 0 & 0 & A_{8,5} & 0 & A_{8,7} & A_{8,8} & A_{8,9} & 0 & A_{8,11} & 0 & 0 & B_{2,8} & 0 & 0 & 0 & 0 & T_{3,\text{out}} \\ 0 & 0 & 0 & 0 & 0 & 0 & A_{9,6} & A_{9,7} & A_{9,8} & A_{9,9} & 0 & A_{9,11} & 0 & B_{2,9} & 0 & 0 & 0 & 0 & T_{3,\text{in}} \\ 0 & 0 & 0 & 0 & 0 & 0 & 0 & 0 & 0 & 0 & 0 & A_{10,10} & A_{10,11} & B_{1,10} & B_{2,10} & 0 & 0 & 0 & T_{\text{ch}} \\ 0 & 0 & 0 & 0 & 0 & 0 & 0 & 0 & 0 & 0 & 0 & 1 & 0 & 0 & 0 & 0 & 0 & 0 & T_{\text{ch}} \\ \hline 1 & 0 & 0 & 0 & 0 & 0 & 0 & 0 & 0 & 0 & 0 & 0 & 0 & 0 & 0 & 0 & 0 & 0 & T_{C_1} \\ 0 & 0 & 0 & 0 & 0 & 0 & 0 & 0 & 0 & 0 & 0 & 0 & 0 & 0 & 0 & 0 & 0 & 0 & T_{\text{ch}} \\ \hline T_{C_1} & T_{1,\text{out}} & T_{1,\text{in}} & T_{C_2} & T_{2,\text{out}} & T_{2,\text{in}} & T_{C_3} & T_{3,\text{out}} & T_{3,\text{in}} & T_{\text{ch}} & T_{\text{ch}} & T_{C_{\text{in}}} & T_{\text{amb}} & & & & & & \end{array} \quad (6)$$

This three-node model represents our system model for a single chamber. At this stage, it is important to note that, for validating the

experimental system dynamics discussed in Section 4, a 10-node model is also used in the simulations. This model is designed to represent and validate the dynamics of a special chamber equipped with a measuring rod that includes 10 separate PT 100 sensors. The 10-node model is constructed using the same lumped modeling approach as the three-node model, by connecting the individual node models.

2.5. Sorbent average temperature estimation

In an industrial-scale DAC system, harsh operating conditions (e.g., high humidity and acidic environments) limit the feasibility of integrating physical temperature sensors directly into the cartridge or adsorbent, along with the costly vacuum feed-through required for instrumentation cabling. The lack of direct measurements limits the precise regulation of the heating process to maintain the desired operating temperature.

To address this issue, we propose a virtual sensor in the form of a linear state estimator to estimate the average temperature of the sorbent inside the cartridge. The system model used for designing the estimator is linearized around an operating temperature of 0.25 pu. An accurate estimate is critical around this temperature range, as a robust estimate is essential for the state change algorithm.

The considered model is an approximation of the cartridge represented by a single node, due to straightforward implementation and the ability to adjust the estimator accordingly with correction coefficients of the model itself. Additionally, to account for the effect of the chamber temperature T_{ch} , an extra state is augmented into the cartridge state-space model, as presented in (4). Consequently, the 1-node estimator is developed into a linear state-space model with a state vector that includes.

$$\mathbf{x} = [T_{C_1} \quad T_{1,\text{out}} \quad T_{1,\text{in}} \quad T_{\text{ch}} \quad T_{\text{ch}}]^T, \quad (7)$$

with following input \mathbf{u} and output \mathbf{y} vectors,

$$\mathbf{u} = [T_{C_{\text{in}}} \quad T_{\text{amb}}]^T, \quad (8)$$

$$\mathbf{y} = [T_{C_{\text{out}}} \quad T_{\text{ch}}]^T. \quad (9)$$

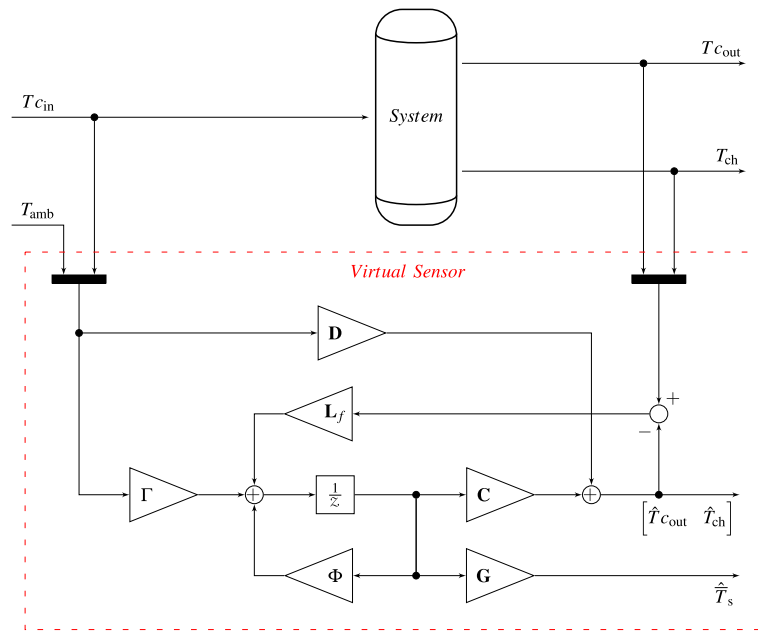


Fig. 5. Generalized block diagram showing the virtual sensor's connection to the chamber of the DAC system, with the main variables presented.

Where T_{amb} is the ambient temperature. When the 1-node cartridge model is combined with the chamber dynamics model, the continuous-time state-space representation used for the estimator design is obtained as follows,

$$\dot{\mathbf{x}} = \begin{bmatrix} A_{11} & A_{12} & A_{13} & 0 & 0 \\ A_{21} & A_{22} & A_{23} & 0 & A_{25} \\ A_{31} & A_{32} & A_{33} & 0 & A_{35} \\ 0 & 0 & 0 & A_{44} & A_{45} \\ 0 & 0 & 0 & 1 & 0 \end{bmatrix} \begin{bmatrix} T_{c1} \\ T_{1,out} \\ T_{1,in} \\ T_{ch} \\ T_{ch} \end{bmatrix} + \begin{bmatrix} B_{11} & 0 \\ 0 & B_{22} \\ 0 & B_{32} \\ B_{41} & B_{42} \\ 0 & 0 \end{bmatrix} \begin{bmatrix} T_{c,in} \\ T_{amb} \end{bmatrix},$$

$$\mathbf{y} = \begin{bmatrix} 1 & 0 & 0 & 0 & 0 \\ 0 & 0 & 0 & 0 & 1 \end{bmatrix} \begin{bmatrix} T_{c1} \\ T_{1,out} \\ T_{1,in} \\ T_{ch} \\ T_{ch} \end{bmatrix} + \begin{bmatrix} 0 & 0 \\ 0 & 1 \end{bmatrix} \begin{bmatrix} T_{c,in} \\ T_{amb} \end{bmatrix}, \quad (10)$$

where, for clarity, the variables A_{11}, B_{11}, \dots , etc., represent the coefficients of the differential equations derived in Section 2.1. The resulting fifth-order model is used to design a discrete-time state estimator, which is given in the standard estimator form as follows,

$$\hat{\mathbf{x}}(k) = \Phi \hat{\mathbf{x}}(k) + \Gamma \mathbf{u}(k) + \mathbf{L}_f (\mathbf{y}(k) - \hat{\mathbf{y}}(k)), \quad (11)$$

$$\hat{\mathbf{y}}(k) = \mathbf{C} \hat{\mathbf{x}}(k) + \mathbf{D} \mathbf{u}(k), \quad (12)$$

where Φ is the discrete system matrix, $\hat{\mathbf{x}}(k)$ is the state estimate vector, Γ is the discrete input matrix, k is the number of sample, \mathbf{C} measurement matrix, \mathbf{D} feedforward matrix, $\hat{\mathbf{y}}(t)$ is a vector for model predictions and \mathbf{L}_f is fixed-parameter estimator (Kalman) gain. Based on the order of the state estimation vector (7), the following matrix is introduced,

$$\mathbf{G} = \begin{bmatrix} 0 & \frac{1}{2} & \frac{1}{2} & 0 & 0 \end{bmatrix}, \quad (13)$$

that is used to form the average temperature estimate \hat{T}_s from the states as follows

$$\hat{T}_s = \mathbf{G} \hat{\mathbf{x}}(k). \quad (14)$$

In Fig. 5, a generalized block diagram representing the sorbent temperature estimation with the proposed estimator (virtual sensor) is shown. The diagram also illustrates its connection to the DAC system chamber, highlighted within a red dashed box.

2.6. State change from circulation to heating

Deciding the optimum point to switch from the heat-circulation phase to the heating-only phase in the cartridge process involves balancing energy savings with process time. Lengthening the circulation phase can save more energy but also extend the overall process duration. The latter can decrease the overall energy-saving benefits because of reduced CO₂ productivity.

Two pseudo-optimal points are illustrated in Fig. 6 for the proposed circulation procedure, where thermal energy is transferred from a hot cartridge to a cold one through a closed loop. The energy conservation scenario's optimal point (black filled circle in Fig. 6) is achieved when the heat transfer rate to the cold cartridge reaches zero after the circulation phase begins. Extending the circulation phase beyond this point leads to additional energy loss, as the cartridge's temperature decreases due to heat losses to the ambient.

In the optimal process scenario, circulation is stopped at the point indicated by the black circle in Fig. 6 when the heat transfer rate to the cold cartridge begins to decrease significantly. In other words, the goal is to maintain the heat transfer rate to the cartridge as high as possible for as long as feasible. Overall, this represents a trade-off between the time spent and the benefits gained from the circulation procedure. For instance, analyzing the response of the cold cartridge in Fig. 6 during the 0 to 60-minute interval, the response can be roughly approximated using a first-order system to step excitation. Consequently, the optimal point can be estimated to be near the time constant of this first-order system. From a process dynamics perspective, this point corresponds to the cold cartridge reaching 63% of its final temperature in the energy conservation scenario.

Calculating the exact 63% point in real-time is not feasible. Therefore, the proposed state selector approach uses an approximation of the heat transfer rate to determine the transition points. The state selector monitors these points during operation and uses a parameter σ to define the desired transition from circulation to heating of the cartridge. Consequently, a state selector module is introduced to facilitate transitions between the circulation and heating phases. The structure of the state selector is illustrated in Fig. 7

The state change module, shown in Fig. 7, features a state selector that determines the transition point from the circulation phase to the heating phase. This transition is managed by an algorithm that analyzes

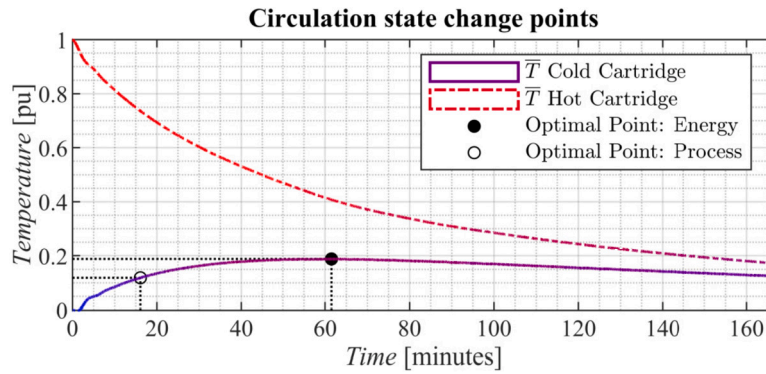


Fig. 6. Temperature responses from the experimental system are shown for when the heated cartridge transfers energy to a cold one. The potential optimal points for state changes are indicated.

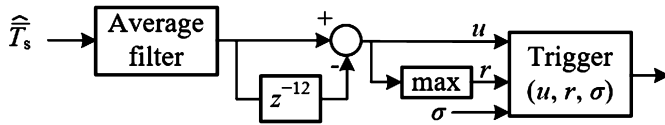


Fig. 7. Structure of the state selector that manages the transition between heating and circulation phases.

the discrete derivative of the sorbent temperature estimate, as provided by the virtual sensor discussed in Section 2.5). The point σ at which the transition occurs can be determined by examining the free circulation step responses from the heated cartridge to the cold one, as shown in Fig. 6. In the state selector approach, the reading from the virtual sensor is filtered using a moving average filter, followed by the calculation of the discrete derivative u with 12 delayed samples (with a sample time of 5 seconds).

The key advantage of using the derivative of the estimate is that it allows the state selector algorithm to operate across different temperature ranges, unlike hard-coded temperature values that trigger state changes at specific temperatures. This leads to a more adaptive system. In the algorithm, r is the maximum value of the discrete derivative, which is also used in the triggering function. The algorithm’s robustness relies heavily on the precision and reliability of the virtual sensor. Different differentiation intervals can reduce the chance of false triggering but may also affect the responsiveness of the state selector module.

3. Cascaded control approach

In this section, a control law is proposed to regulate the system between the process phases described in section 2. The cascade control law uses an inner controller for the TES and an outer PI-control loop for regulating the sorbent temperature. The block diagram of the proposed control law is shown in Fig. 8, illustrating the relevant control functionalities. The PI controllers are implemented in their standard form.

$$C(s) = K_p \cdot \left(1 + \frac{1}{T_i \cdot s} \right), \quad (15)$$

with proportional gain K_p and integration time T_i . The principle of the inner control used in the constant power heating element is based on turning the heating element on and off with varying duty cycle D_h , and its feedback is T_h , the heater liquid temperature. The outer PI-control loop’s reference is the target operating temperature T_{op} , which is compared to the average temperature estimate \hat{T}_s .

The preliminary tuning of the outer and inner PI-controllers is based on the SIMC tuning principle presented by Grimholt and Skogestad (2012) using simplified models for TES and cartridge dynamics. For the outer controller, the nominal gains were determined as $K_p = 1.26$ and $T_i = 1380$ s. These values are considered later on as nominal values for

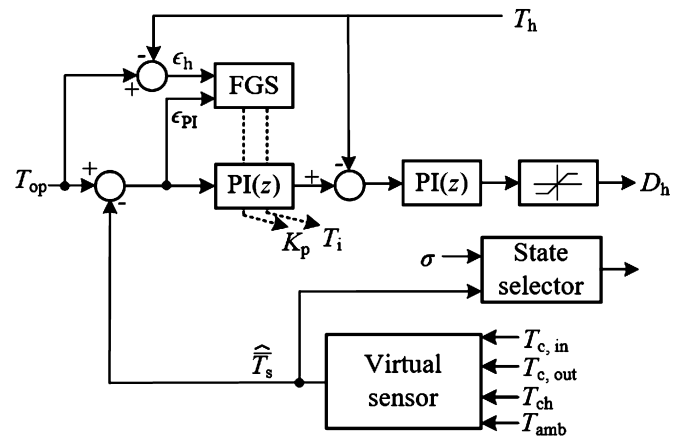


Fig. 8. Block diagram of the proposed cascade control law for heating with the FGS and virtual sensor.

the FGS update routine. The proposed control law includes a fuzzy gain scheduler (FGS) that is used with the outer PI-controller of the cascade controller. This approach has been selected to address the slow heating dynamics of the system and to prevent excessive overshoot of the response, thereby ensuring good control robustness.

The controller’s proportional gain K_p and integration time T_i are actively tuned online using routines similar to those shown in Honkanen et al. (2019). The parameters provided by the FGS are constrained within certain limits based on the desired controller behavior and system dynamics. Considering the control targets of the system, the natural choice for the feedback parameter used in the FGS is the sorbent temperature estimate, as the system does not directly measure the sorbent temperature.

As shown in Fig. 8, the FGS uses the error (denoted as ϵ_{PI}) between the estimate and the operational temperature of the sorbent. The second parameter used in the FGS is the error of the liquid temperature in the TES from the operational temperature of the sorbent, denoted as ϵ_h . The liquid temperature is used to link the control to the liquid temperature to prevent a situation where too hot liquid would be passed into the system, which could lead to the degradation of the sorbent itself.

3.1. Fuzzy gain scheduler (FSG)

This section explores gain scheduling as a method to enhance the responsiveness of the system by employing the Fuzzy Gain Scheduling (FGS) principle within a PI controller structure, to surpass the performance of a PI controller with fixed gains. While aggressive tuning of a fixed-gain controller might improve responsiveness, it often results in undesirable overshoot, which is problematic for this application.

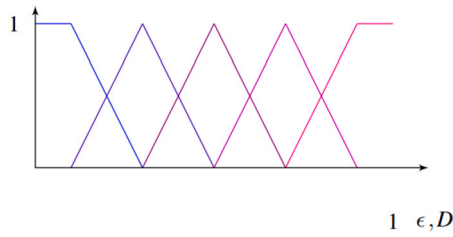


Fig. 9. Illustration of triangular membership functions (MFs) from functions.

Table 1

The fuzzy tuning rule derived for proportional gain K_p .

K_p		ϵ_{PI}				
		-B	-S	Z	+S	+B
ϵ_h	-B	3	2	2	1	1
	-S	3	2	2	1	1
	Z	3	2	2	1	1
	+S	2	2	2	2	1
	+B	2	2	2	2	1

Table 2

The fuzzy tuning rule for integration time T_i .

T_i		ϵ_{PI}				
		-B	-S	Z	+S	+B
ϵ_h	-B	1	2	2	2	1
	-S	1	2	2	2	1
	Z	1	2	2	2	2
	+S	2	2	2	2	3
	+B	2	2	2	2	3

An alternative approach, such as employing feed-forward structures, could be used to increase the control input during times when more reactive behavior is desired. However, suitable feed-forward structures are not discussed in detail in this paper, so the focus remains on the Fuzzy Gain Scheduling (FGS) principle.

The fuzzification of the input variables is accomplished by using triangular membership functions (MFs), as depicted in Fig. 9. The corresponding membership weights are represented in vector form.

$$\sigma_{MF} = [w_1 \ w_2 \ w_3 \ w_4 \ w_5] \quad (16)$$

The weights $w_1 \dots w_5$ are related to the particular membership. The membership functions must be fitted according to the following condition that $\sum_{i=1}^5 w_{MF,i} = 1$ as denoted by Zhao et al. (1993). The weights obtained from the membership functions are then combined with predefined instructions stored in specific instruction tables. These tables contain instructions represented by integer values ranging from 1 to 3. The instruction table for the proportional gain K_p is shown in Table 1, while the instructions for the integration time T_i are provided in Table 2.

The combination of the weights and instructions is done by multiplication in the inference engine. The following considerations are made when the instruction table is assumed to be in matrix form to define a gain K_{inst} .

$$\sum_{j=1}^5 \sum_{i=1}^5 \sigma_{MF,\epsilon_{PI}}(i) \cdot \sigma_{MF,\epsilon_h}(j) \cdot T_{inst}(j,i) = K_{inst} \quad (17)$$

where $T_{inst}(j,i)$ represent a value located at (i,j) in the instruction table. The inference engine results in gains that have values between 1 to 3 according to the instructions. In this case, the gains are scaled back to range from 0 to 1 to be used with designed output membership functions to introduce a new degree of freedom to the FGS design. Inverse sigmoidal functions are used as output functions to ensure linear op-

Table 3

Fuzzy gain scheduler gain boundaries (High and Low) and controller nominal (Nom / fixed) gains, when controller is driven without FGS.

Controller gains		
	K_p	T_i [s]
Low	1.19	1150
High	1.33	1620
Nom / Fixed	1.26	1380

eration near the region where the controller gains conduct to a robust system. The following equations (18) and (19), represent the derived output membership functions,

$$f(x) = \begin{cases} y = 1, & \text{if } x < p_1, \\ y = 0.1 \cdot \log\left(\frac{x}{1-x}\right) + 0.5, & \text{if } p_1 \leq x \leq p_2, \\ y = 0, & \text{if } x > p_2, \end{cases} \quad (18)$$

$$f(x) = \begin{cases} y = 0, & \text{if } x < p_1, \\ y = 0.5 - 0.1 \cdot \log\left(\frac{x}{1-x}\right), & \text{if } p_1 \leq x \leq p_2, \\ y = 1, & \text{if } x > p_2, \end{cases} \quad (19)$$

where p_1 and p_2 are bounds to the functions. Since these functions are logarithmic, it is important to consider their rapid decrease or growth near the bounds of 0 and 1. For this case, the specific values of $p_1 = 0.01$ and $p_2 = 0.99$ were selected to prevent situations when the result would be infinite.

The solution obtained from the output membership functions is scaled back to real values for use in the PI controller. As mentioned previously, the controller gains are constrained to a certain range. Therefore, the following approach is used,

$$K_p = K'_p \cdot (K_{p,Hi} - K_{p,Lo}) + K_{p,Lo} \quad (20)$$

$$T_i = T'_i \cdot (T_{i,Hi} - T_{i,Lo}) + T_{i,Lo} \quad (21)$$

where K'_p and T'_i are the controller's proportional gain and integration time. The values $K_{p,Hi}$ and $K_{p,Lo}$ represent the high and low limits for the proportional gain, while $T_{i,Hi}$ and $T_{i,Lo}$ represent the high and low limits for the integral action.

The gain scheduler boundaries are shown in Table 3, with the nominal controller gains calculated based on the SIMC tuning rule. The derivation of the suitable boundaries is based on desired system behavior and chosen output functions, and these were selected based on simulations and tests using the experimental system.

Similarly, the table shows the controller gains used for the fixed-gain controller under the "Nom / Fixed" row.

4. Experimental results

In this section, the open-loop responses of a 10-node simulation model are compared with the measured responses from an experimental system with a horizontal temperature distribution of the test cartridge, at various time steps during open-loop heating. The performance of the virtual sensor and the fixed-gain PI controller is validated through a validation cycle, and the effect of implementing Fuzzy Gain Scheduling (FGS) on the controller is demonstrated. Finally, the focus shifts to analyzing the energy consumption when the process is operated with different strategies.

4.1. Validation of the modeling approach

The model is validated by comparing the simulation results with experimental data from a step change in the hot water temperature (from 0 to 1 pu) and the inlet flow (from 0 to 1 pu). The results are shown

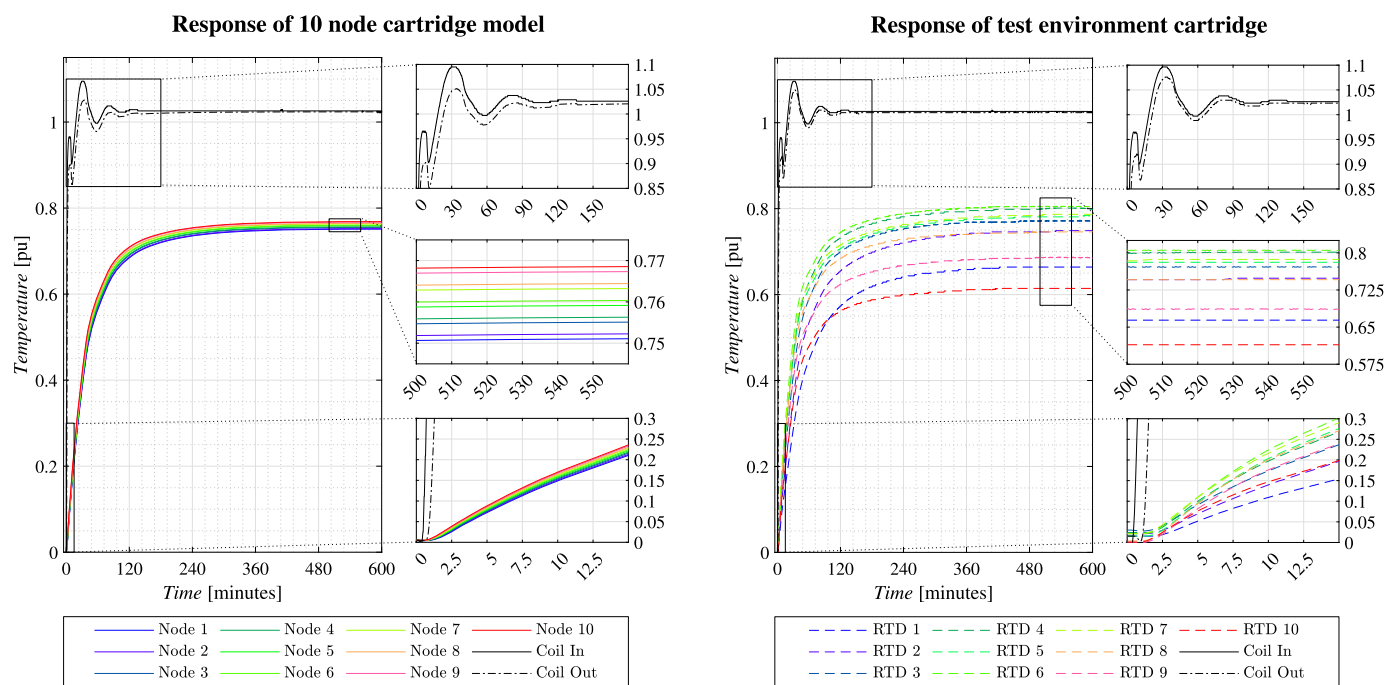


Fig. 10. a) Simulated open loop temperature step response of chamber modeled with 10 node model in Simulink environment and b) measured temperatures of the cartridge of the experimental system with the integrated measurement rod. In the legend, the RTD prefix means resistance temperature detectors (PT 100) number in the measurement rod. The sensor numbering is done according to the stacked node approach, e.g., RTD 10 locates at the bottom of the cartridge (corresponding to 10th node), and RTD 1 is at the top (corresponding to 1st node). Flow of heat transfer medium in spiral coil is from bottom to top.

in Fig. 10, where the simulated response is depicted on the left and the measured one on the right, respectively.

The simulated results show slight temperature variations between nodes, likely due to heat transfer from the previous node's coil to the sorbent. The measured temperature responses exhibit similar fundamental dynamic behavior to the simulations, though with some deviation. Notably, the measured temperatures at the end sensors (located at nodes 1, 2, and 9, 10) are lower than those at the middle nodes. This difference can be attributed to the cartridge housing. Since the cartridge is housed within a steel chamber, the metallic supports create a good conductive path for heat to dissipate from the sorbent.

It is also seen that in the simulation model temperature drop through the cartridge is slightly higher than the measured response, indicating some inaccuracies in the model's internal heat transfer phenomenon. Especially when a wider spread of node temperatures in the measured response is compared to the simulated response. Fig. 11 illustrates the steady-state temperature distribution across the horizontal axis of the cartridge at various points during similar open-loop heating scenarios described in Fig. 10. These observations highlight the significant impact of the metal frame and brackets on the cartridge's thermal distribution.

The temperature distribution after the first hour of heating ($t = 60$ min) shows that the center of the cartridge heats up faster than the ends. This is likely due to heat loss through the cartridge supports to the surrounding chamber. After 9 hours, the temperatures reach a steady state, as shown in Figs. 10 and 11, with a distribution profile similar to that observed after one hour. As the DAC chamber temperature increases, heat losses to the chamber decrease slightly, as indicated by a wider hot band in the profile, especially at the top of the cartridge (sensors 1 to 5).

Despite some differences due to unmodeled dynamics and imperfections, the simulations and actual measurements exhibit similar dynamic behavior. This similarity suggests that the presented modeling approach captures the essential aspects of the system's thermal behavior.

4.2. Performance of the closed-loop control and estimator

The performance of the proposed virtual sensor for estimating the average temperature of the sorbent, along with the derived control laws, is studied using the test cartridge that includes a temperature measurement rod placed horizontally in the middle of the outer sorbent mass. This test is conducted by considering a complete operation cycle of the testing environment shown in Fig. 12. The cycle begins with heat circulation from one cartridge to the cartridge with the temperature measurement rod.

For the validation test, the cartridge undergoes several steps. First, it is heated using heat circulation from a hot cartridge for 0 to 50 minutes. This is followed by further heating with TES to reach the desired operational temperature from 50 to 650 minutes. The next step involves cooling using heat circulation from a cold cartridge, occurring between 650 and 700 minutes. Finally, cooling to ambient temperature is achieved using a radiator from 700 minutes onward.

When comparing the estimation to the measured average temperature, it can be seen that these are in good agreement with each other indicating that the proposed one-node estimator can produce a reasonable estimate, when the model includes properly adjusted correction coefficients discussed in the supplementary material.

Next, the proposed control law is validated by examining the heating phase using the FGS updating scheme. Fig. 13a shows the PI-controller parameters updated by the FGS. Meanwhile, Fig. 13b illustrates the dynamics of the TES and sorbent temperatures for both the FGS-disabled and FGS-enabled cases.

It is noted that Fig. 13b represents two results; step responses of the cascaded control when the FGS is disabled (left) and enabled (right). When looking at the results with the FGS, it can be noticed that during the early phase of the heating, both the proportional and integral gains of the PI-controller have higher and lower values to speed up the heating rate. Also when the error between the reference and sorbent temperature estimate is converging towards a value close to zero, it is seen that the FGS will update the controller gain values to less aggressive values. On the contrary, by looking at the case without FGS it is seen that the

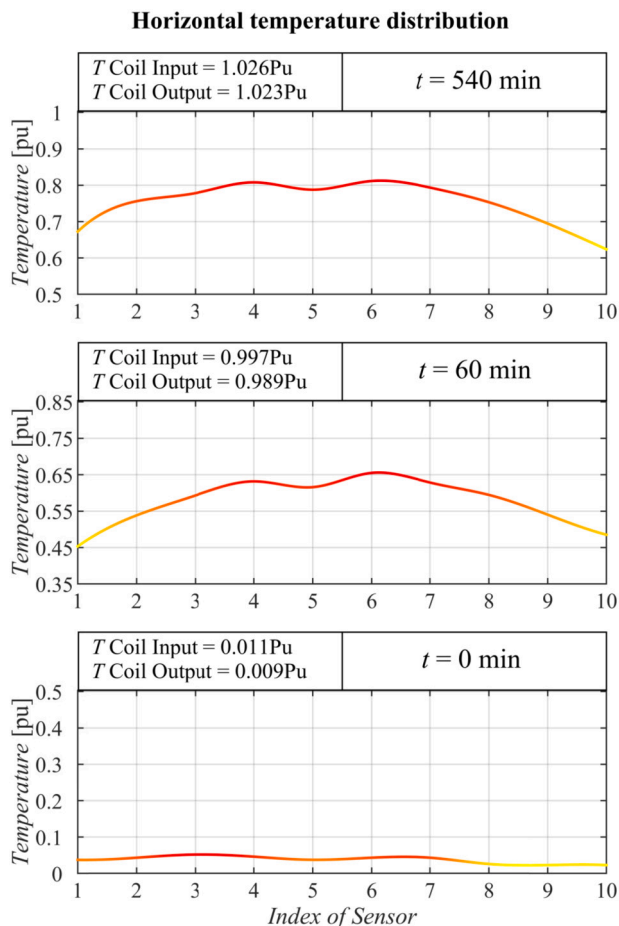


Fig. 11. The temperature gradient of the cartridge along the horizontal axis is shown. The results are taken from a steady-state situation when the cartridge coil is fed with water at a temperature of 1 pu. In the figure, yellow shades represent lower temperatures, while red shades indicate higher temperatures.

heating takes a longer time to reach the target temperature indicating clearly that the FGS approach can improve the process dynamics.

4.3. Analysis of energy consumption

Energy savings achieved through the proposed circulation phase and FGS implementation in a cascaded PI controller were assessed by comparing energy consumption across four distinct test scenarios with a standard fixed-gain PI controller that lacks a circulation phase. Case I serves as the baseline, involving a fixed-gain PI controller without a circulation phase. In Case II, FGS is activated, and the state selector transitions from circulation to heating near the process's optimal point, as shown in Fig. 6. Case III also activates FGS, but the state selector shifts from circulation to heating near the energy optimal point. Finally, Case IV examines the scenario where FGS is deactivated, and the controller operates with fixed gains, with the state selector moving from circulation to heating near the energy optimal point. During the test cases, the ambient temperature was maintained within a range of $23.5^{\circ}\text{C} \pm 0.75^{\circ}\text{C}$.

The performance of Cases I-IV is evaluated by comparing energy savings and the total duration of the circulation/heating phase. Energy consumption was measured using a Lovato DMED301 energy meter, with measurements starting at the beginning of the circulation phase or, for Case I where circulation is not utilized, at the start of heating. Measurements are concluded when the adsorbent temperature reaches 95% of its steady-state value. The results of these tests, as shown in Fig. 14 are compared against Case I.

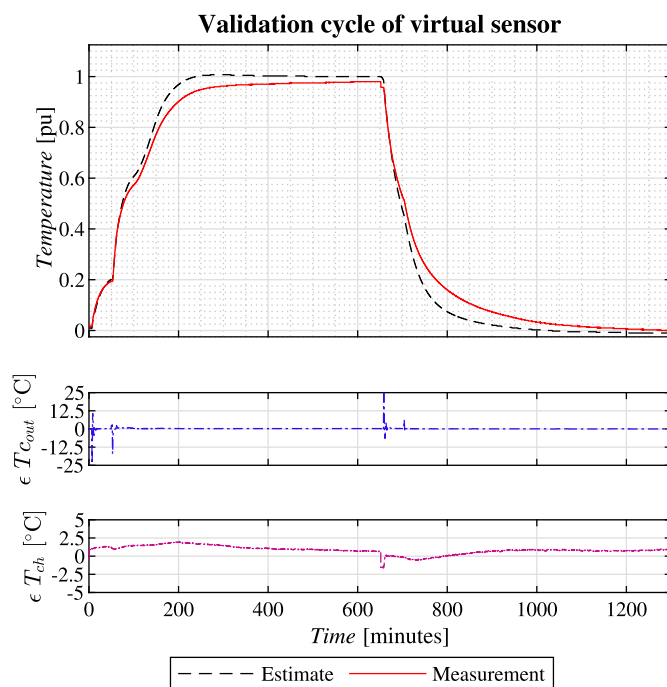


Fig. 12. The measured average temperature is compared to the estimated temperature during a complete cycle of circulation, heating, and cooling of one cartridge in the test system under closed-loop control.

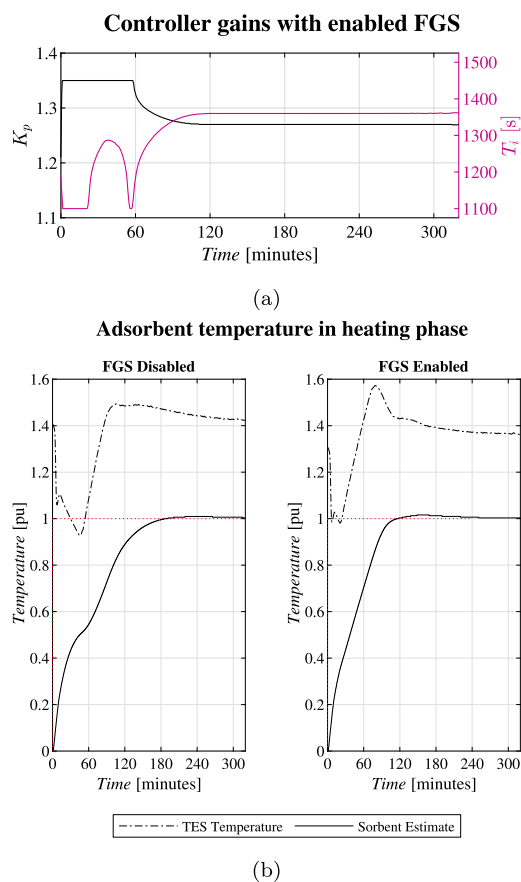


Fig. 13. a) Updated control parameters during the heating phase and b) sorbent temperature under closed-loop control.

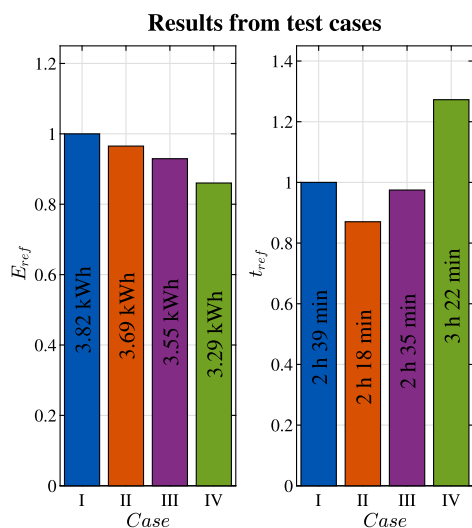


Fig. 14. Energy consumption and elapsed time of heating/circulation phases during test cases I-IV.

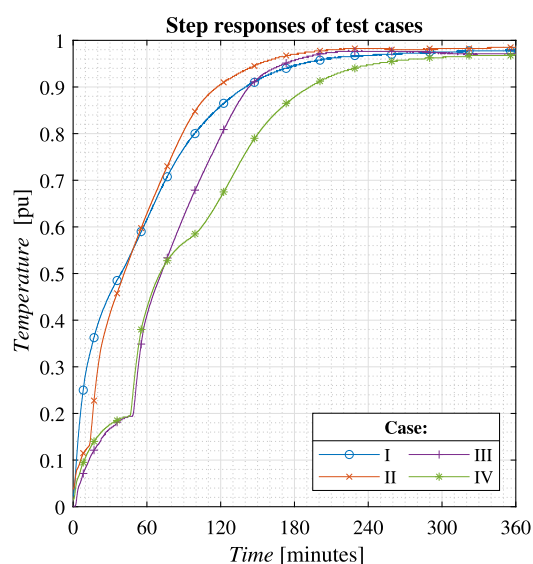


Fig. 15. Measured step responses from test cases I-IV.

Comparing Case II with the reference case shown in Fig. 14, energy consumption is reduced to 96.6%, and heating time is decreased by 21 minutes. This improvement results from the more aggressive FGS-driven controller gains, which increase TES temperatures and enhance heat transfer.

In Case III, energy consumption is reduced to 92.9% of that in the reference case, with heating time remaining nearly identical to the reference. Since heating is just one step in the entire DAC process, it is not feasible to extend the heating period indefinitely if the entire process must be completed within a specific time frame. Thus, Case III illustrates the potential of combining the proposed circulation procedure with FGS to achieve energy savings while maintaining the reference heating time.

Finally, in Case IV, where FGS is disabled and a fixed-gain controller is used, energy consumption is reduced to 86.1% of that in the reference case. However, the heating time increases by 43 minutes. Prolonging the heating period could impact the overall productivity of the DAC process, such as daily productivity, potentially offsetting the energy savings achieved with this control strategy.

Fig. 15 illustrates the step responses for different cases. The most notable effect of FGS is observed between Cases III and IV, particu-

larly after the adsorbent reaches approximately 0.55 pu. As shown in Fig. 13b, the FGS PI-controller addresses the sluggish heating behavior by increasing the TES temperature reference earlier in the heating phase. This adjustment enables the TES temperature to reach higher levels, which enhances the heat transfer rate to the cartridge.

5. Conclusions

In this work, we demonstrated that node-based modeling of DAC cartridges effectively captures the dynamics of sorbent heating.

Additionally, we developed and validated a virtual sensor based on a single-node model. This virtual sensor accurately represents temperature changes within the cartridge across different phases of the process, including heat re-circulation, heating, and cooling stages. Due to its accuracy, the virtual sensor was subsequently used as feedback for the proposed cascade control law incorporating FGS.

We also showed that FGS-based control accelerates the heating rate and provides a more nuanced approach to influencing system responses.

Overall, the proposed heat circulation method and FGS-based control demonstrate significant potential in reducing overall thermal energy usage, which is crucial for the effective implementation of DAC technology.

CRediT authorship contribution statement

Antti Paajanen: Writing – original draft, Visualization, Validation, Software, Methodology, Investigation, Conceptualization. **Niko Nevaranta:** Writing – review & editing, Writing – original draft, Visualization, Supervision. **Cyril Bajamundi:** Writing – review & editing, Writing – original draft, Visualization, Supervision.

Declaration of competing interest

The authors declare the following financial interests/personal relationships which may be considered as potential competing interests: Antti Paajanen reports financial support was provided by Soletair Power. Antti Paajanen reports a relationship with Soletair Power that includes: employment. co-author had employment with Soletair Power - Cyril Bajamundi.

Data availability

The authors do not have permission to share data.

Appendix A. Supplementary material

Supplementary material related to this article can be found online at <https://doi.org/10.1016/j.ces.2024.120745>.

References

- An, K., Farooqui, A., McCoy, S.T., 2022. The impact of climate on solvent-based direct air capture systems. *Appl. Energy* 325, 119895. <https://doi.org/10.1016/j.apenergy.2022.119895>. <https://www.sciencedirect.com/science/article/pii/S0306261922011588>.
- Bacocchi, R., Storti, G., Mazzotti, M., 2006. Process design and energy requirements for the capture of carbon dioxide from air. *Chem. Eng. Process. Process. Intensif.* 45, 1047–1058. <https://doi.org/10.1016/j.ces.2006.03.015>. <https://www.sciencedirect.com/science/article/pii/S0255270106000791>.
- Bastida, H., Ugalde-Loo, C.E., Abeysekera, M., Qadrdan, M., Zhong Wu, J., Jenkins, N., 2019. Dynamic modelling and control of thermal energy storage. *Energy Proc.* 158, 2890–2895. <https://www.sciencedirect.com/science/article/pii/S1876610219309890>. *Innovative Solutions for Energy Transitions*.
- Bird, T.J., Jain, N., 2020. Dynamic modeling and validation of a micro-combined heat and power system with integrated thermal energy storage. *Appl. Energy* 271. <https://www.sciencedirect.com/science/article/pii/S0306261920304670>.
- Cao, L., 2021. Application of artificial intelligence on the CO₂ capture: a review. *J. Therm. Anal. Calorim.* 145, 1751–1768. <https://doi.org/10.1007/s10973-021-10777-4>.

- Chen, Y.-H., Shen, M.-T., Chang, H., Ho, C.-D., 2019. Control of solvent-based post-combustion carbon capture process with optimal operation conditions. *Processes* 7. <https://doi.org/10.3390/pr7060366>. <https://www.mdpi.com/2227-9717/7/6/366>.
- Grimholt, C., Skogestad, S., 2012. Optimal pi-control and verification of the simc tuning rule. *IFAC Proc. Vol.* 45, 11–22. <https://doi.org/10.3182/20120328-3-IT-3014-00003>. <https://www.sciencedirect.com/science/article/pii/S1474667016309934>.
- Gutierrez-Ortega, A., Melis, A., Nomen, R., Sempere, J., Fernandez-Garcia, J., Pou, J., Gonzalez-Olmos, R., 2023. Parameter screening of a vpsa cycle with automated breakthrough control for carbon capture. *Fuel* 339, 127298. <https://doi.org/10.1016/j.fuel.2022.127298>. <https://www.sciencedirect.com/science/article/pii/S0016236122041229>.
- Honkanen, J., Hannonen, J., Korhonen, J., Nevaranta, N., Silventoinen, P., 2019. Non-linear pi-control approach for improving the dc-link voltage control performance of a power-factor-corrected system. *IEEE Trans. Ind. Electron.* 66, 5456–5464. <https://doi.org/10.1109/TIE.2018.2868282>.
- House, K.Z., Baclig, A.C., Ranjan, M., van Nierop, E.A., Wilcox, J., Herzog, H.J., 2011. Economic and energetic analysis of capturing CO₂ from ambient air. *Proc. Natl. Acad. Sci.* 108, 20428–20433. <https://doi.org/10.1073/pnas.1012253108>.
- Jiang, N., Shen, Y., Liu, B., Zhang, D., Tang, Z., Li, G., Fu, B., 2020. CO₂ capture from dry flue gas by means of vpsa, tsa and tvsa. *J. CO₂ Util.* 35, 153–168. <https://doi.org/10.1016/j.jcou.2019.09.012>. <https://www.sciencedirect.com/science/article/pii/S2212982019303233>.
- Keith, D.W., Holmes, G., Angelo, D.St., Heidel, K., 2018. A process for capturing CO₂ from the atmosphere. *Joule* 2, 1573–1594. <https://doi.org/10.1016/j.joule.2018.05.006>.
- Lai, J.Y., Ngu, L.H., Hashim, S.S., 2021. A review of CO₂ adsorbents performance for different carbon capture technology processes conditions. *Greenh. Gases Sci. Technol.* 11, 1076–1117. <https://doi.org/10.1002/ghg.2112>.
- Lindh, T., Nevaranta, N., 2020. Automatized method of moments to estimate process model of diesel engine dynamics. In: 2020 25th IEEE International Conference on Emerging Technologies and Factory Automation (ETFA), vol. 1, pp. 1201–1204.
- Nash, A.L., Badithela, A., Jain, N., 2017. Dynamic modeling of a sensible thermal energy storage tank with an immersed coil heat exchanger under three operation modes. *Appl. Energy* 195, 877–889. <https://doi.org/10.1016/j.apenergy.2017.03.092>.
- National Academies of Sciences Engineering Medicine, 2019. Negative Emissions Technologies and Reliable Sequestration: A Research Agenda. The National Academies Press, Washington, DC.
- Parvazinia, M., Garcia, S., Maroto-Valer, M., 2018. CO₂ capture by ion exchange resins as amine functionalised adsorbents. *Chem. Eng. J.* 331, 335–342. <https://doi.org/10.1016/j.cej.2017.08.087>. <https://www.sciencedirect.com/science/article/pii/S1385894717314316>.
- Salvinder, K., Zabiri, H., Taqvi, S.A., Ramasamy, M., Isa, F., Rozali, N., Suleman, H., Maulud, A., Shariff, A., 2019. An overview on control strategies for CO₂ capture using absorption/stripping system. *Chem. Eng. Res. Des.* 147, 319–337.
- Stampi-Bombelli, V., van der Spek, M., Mazzotti, M., 2020. Analysis of direct capture of CO₂ from ambient air via steam-assisted temperature–vacuum swing adsorption. *Adsorption* 26, 1183–1197. <https://doi.org/10.1007/s10450-020-00249-w>.
- Wu, X., Shen, J., Li, Y., Wang, M., Lawal, A., Lee, K.Y., 2018. Nonlinear dynamic analysis and control design of a solvent-based post-combustion CO₂ capture process. *Comput. Chem. Eng.* 115, 397–406. <https://doi.org/10.1016/j.compchemeng.2018.04.028>. <https://www.sciencedirect.com/science/article/pii/S0098135418303831>.
- Wu, X., Wang, M., Liao, P., Shen, J., Li, Y., 2020. Solvent-based post-combustion CO₂ capture for power plants: a critical review and perspective on dynamic modelling, system identification, process control and flexible operation. *Appl. Energy* 257, 113941. <https://doi.org/10.1016/j.apenergy.2019.113941>. <https://www.sciencedirect.com/science/article/pii/S0306261919316289>.
- Zhao, Z.-Y., Tomizuka, M., Isaka, S., 1993. Fuzzy gain scheduling of pid controllers. *IEEE Trans. Syst. Man Cybern.* 23, 1392–1398. <https://doi.org/10.1109/21.260670>.